Dynamics of a high-Reynolds-number bubble rising within a thin gap

Véronique Roig, Matthieu Roudet, Frédéric Risso, Anne-Marie Billet

Dynamics of a high-Reynolds-number bubble rising within a thin gap

By VÉRONIQUE ROIG [1,3]
MATTHIEU ROUDET [1,2,3]
FRÉDÉRIC RISSO [1,3]
ANNE-MARIE BILLET [2,3]

1 Institut de Mécanique des Fluides de Toulouse, Université de Toulouse (INPT, UPS) and CNRS. Allée C. Soula, Toulouse, 31400, France.
2 Laboratoire de Génie Chimique, Université de Toulouse (INPT,UPS) and CNRS. 4 allée E. Monso, BP74233, Toulouse cedex 4, 31432, France.
3 Fédération de recherche FERMaT, CNRS, allée C. Soula, Toulouse, 31400, France

We report an experimental analysis of path and shape oscillations of an air bubble of diameter d rising in water at high Reynolds number in a vertical Hele-Shaw cell of width h. Liquid velocity perturbations induced by the relative movement have also been investigated to analyze the coupling between the bubble motion and the wake dynamics. The confinement ratio h/d is lower than unity so that the bubble is flattened in between the walls of the cell. As the bubble diameter is increased, the Archimedes and the Bond numbers increase within $10 \leqslant Ar \leqslant 10^4$ and $6 \times 10^{-3} \leqslant Bo \leqslant 140$. Mean shapes become more and more elongated. They first evolve from in-plane circles to ellipses, then to complicated shapes without fore-aft symmetry and finally to semi-circular capped bubbles. The scaling law $Re = 0.5Ar$ is however valid for a large range of Ar, indicating that the liquid films between the bubble and the walls do no contribute significantly to the drag force exerted on the bubble. The coupling between wake dynamics, bubble path and shape oscillations evolves and a succession of contrasted regimes of oscillations is observed. The rectilinear bubble motion becomes unstable from a critical value Ar_1 through an Hopf bifurcation while the bubble shape is still circular. The amplitude of path oscillations first grows as Ar increases above Ar_1 but then surprisingly decreases beyond a second Archimedes number Ar_2. This phenomenon, observed for steady ellipsoidal shape with moderate eccentricity, can be explained by the rapid attenuation of bubble wakes caused by the confinement. Shape oscillations around a significantly elongated mean shape starts for $Ar \geqslant Ar_3$. The wake structure progressively evolves due to changes in the bubble shape. After the break-up of the fore-aft symmetry, a fourth regime involving complicated shape oscillations is then observed for $Ar \geqslant Ar_4$. Vortex shedding disappears and unsteady attached vortices coupled to shape oscillations trigger path oscillations of moderate amplitude. Path and shape oscillations finally decrease when Ar is further increased. For $Ar \geqslant Ar_5$, capped bubbles followed by a steady wake rise on a straight path.

1. Introduction

It is well-known that a large bubble does not usually rise on a straight line but that its velocity and shape may perform oscillations. In general, the dynamics involve the coupling between the instability of the wake and the bubble degrees of freedom associated to its translation, rotation and deformation. Due to the difficulty of measuring or simulating an oscillating bubble, most studies have focused on the determination of averaged characteristics: mean rise velocity and shape (Maxworthy (1996), Magnaudet & Eames (2000)). In the last decade, three-dimensional high-speed imaging (Ellingsen & Risso (2001); Shew *et al.*(2006)) and DNS (Mougin & Magnaudet (2002), Mougin & Magnaudet (2006)) have been used to investigate the unsteady motion of an oblate spheroidal bubble of steady shape rising in an unbounded fluid. The cause of path oscillations is the instability of the wake that develops in a series of symmetry breakdowns leading successively to zig-zag and ellipsoidal paths. Mougin & Magnaudet (2002) also revealed that several types of transitions from straight to oscillatory trajectories may happen, the nature of the bifurcation being highly dependent on the way shape eccentricity or Reynolds number are varied around cross critical points. In their experiments, Lunde & Perkins (1998) also demonstrated that some coupling between shape and path oscillations may occur for freely rising ellipsoidal bubbles. Even when the path instability is primarily excited by the wake, we still therefore have to explore how the shape oscillations respond to the wake instability: What are the conditions of existence of shape oscillations? How do they interact with vortex shedding and path oscillations? How is energy distributed between path and shape oscillations? In the present study we investigate these questions for high-Re bubbles confined between two plates, a flow configuration which is a two-dimensional counterpart of the general problem of the motion of high-Re bubbles free to move in an unbounded space.

Let us consider the general problem of a bubble of equivalent diameter d rising in a vertical Hele-Shaw cell of width h filled with a liquid at rest (fig. 1-a). The non-dimensionnal numbers that control the dynamics are the confinement ratio h/d, the Archimedes number $Ar = \sqrt{gd}d/\nu$ and the Bond number $Bo = \rho g d^2/\sigma$ (where d is defined from the volume ϑ of the bubble by $d = \sqrt{4\vartheta/(h\pi)}$, g is gravity acceleration, ν the kinematic viscosity of the liquid, ρ its density and σ its surface tension). To discuss the bubble dynamics it is also useful to consider the Reynolds number $Re = V_b d/\nu$ based on the mean bubble velocity V_b. The analysis of Navier-Stokes equations describing the flow around a bubble in the thin gap ($h/d << 1$) reveals the existence of two regimes. The ratio of the magnitude of the inertial stress corresponding to the motion within the cell plane to that of the stress in the transverse direction z is $Re(h/d)^2$. The classic Hele-Shaw regime corresponds to $Re(h/d)^2 << 1$ and $Re >> 1$. In contrast, when $Re(h/d)^2 >> 1$ and $Re >> 1$ the in-plane flow is equivalent to a two-dimensional high-Re flow, hereafter referred to as the inertial regime. After the pioneering work of Taylor & Saffman (1959), many studies have been devoted to the Hele-Shaw regime (see Maruvada & Park (1996), and references therein). The present investigation focuses on the inertial regime.

The confinement has some features that alter the bubble dynamics: (i) thin liquid films exist between the bubble and the walls, (ii) bubble deformation is easier along in-plane directions than in the transverse direction so that the bubble degrees of freedom are reduced, (iii) the wake of the bubble is submitted to shear stress at the wall. The dynamics of a bubble in the plane of the cell however allows the study of the coupling and the interplay between path and shape oscillations in regimes where inertia is important, like in unconfined cases. Surprisingly, bubble oscillations in such a regime have not been investigated in details. The mean bubble velocity and shape have been investigated

for very large bubbles (Collins (1965), Lazarek & Littman (1974), Bessler & Littman (1987)). These studies focused on the description of the dynamics of these bubbles in the potential flow regime, calculating their mean velocity and discussing the pressure distribution in the wake. Bush & Eames (1998) experimentally investigated two-dimensional bubbles confined between two plates to determine how the volume of liquid displaced is related to added-mass. Kelley & Wu (1997) focused on the path instability, showing that the critical Reynolds number for the appearance of the instability of the motion increases when the confinement is stronger. But they only considered the case of bubbles of fixed shape at low Bond numbers. In the present contribution, we investigate path and shape oscillations of confined bubbles at large Reynolds number for a large range of flow conditions.

The paper is organized as follows. Section 2 describes the experimental set-up, operating conditions and measurement methods. Section 3 presents the scaling laws obtained for the mean shape and the mean velocity of the bubbles. Section 4 focuses on the wake structure. Finally, section 5 describes bubble shape and path oscillations, which are excited by vortex shedding within the wake.

2. Experimental methods

A single air bubble is injected at the bottom of a vertical Hele-Shaw cell filled with distilled water at ambient temperature. Except that we regularly renew the distilled water, we do not take special care to avoid interface contamination. The cell consists of two glass plates, 40 cm wide, 80 cm high and 8 mm thick, separated by a gap of thickness h =1mm (figure 1-a). We can vary the volume ϑ of the bubble in the range from 0.5 to 700 mm^3 using a syringe equipped with various capillary needles of inner diameters from 0.14 to 0.25 mm. This allows to explore a large range of Archimedes numbers ($10 \leqslant Ar \leqslant 15.10^3$). Since we use a single couple of fluids, the Bond number is not independent of the Archimedes number and evolves as $Bo \approx Ar^{4/3}$ (Fig. 2). It becomes greater than unity from $Ar \approx 440$, so that bubbles of increasing size become more and more deformable, and reaches 140 for the largest bubbles. The ratio of confinement decreases with the Archimedes number: $h/d \approx Ar^{-2/3}$. For h/d smaller than unity ($Ar \geqslant 100$), the bubble deforms and thin liquid films are formed between the bubble interface and the cell walls. When $h/d < 0.5$ ($Ar > 280$), the bubble becomes strongly flattened and a two-dimensional description of the flow becomes pertinent. The liquid and bubble motions are observed in a window located in the central region of the cell, far from the injection and from the upper free surface. The size of this measurement window is varied between 4.3cm×3.4cm and 12.8cm×10.2cm to adapt the field of view to the size of the bubble. The width of the cell was checked by laser beam refraction and proved to be constant over the whole measurement window.

The liquid velocity *a priori* depends on the three space coordinates x, y, z, and time t. However, except in the near vicinity of its interface, the liquid velocity perturbation induced by the motion of a bubble has no component perpendicular to the walls. We developed a specific experimental methodology to measure by means of Particle Image Velocimetry (PIV) the liquid velocity, $\vec{u}(x, y, t) = u\vec{e}_x + v\vec{e}_y$, averaged over the gap (Roudet *et al.* (2011)). The present PIV method uses laser lighting of the whole cell volume and a front camera with a depth of field larger than the gap. Neutrally-buoyant particles made of encapsulated B-Rhodamine are used as fluorescent tracers. Their size is far smaller than the width of the gap. As the whole depth of the flow is illuminated, all the tracers contribute to PIV measurements. Their spatial distribution across the

gap therefore strongly determines their contribution to the velocity estimated by PIV. A non uniform velocity in the z-direction could cause inertial migration of the tracers due to the effect described by Segré & Silberberg (1962). But we have checked that no significant tracer migration occurred here during data acquisition and proved that PIV measurements correspond to the liquid averaged over the gap (Roudet *et al.* (2011)). We used a Quantel multipulse Nd:YAG laser of 2×200mJ, a PCO 12-bits CCD camera (1280×1024 pixels) and the software *PIVIS* developed at IMFT, which is based on an iterative multi-pass PIV algorithm. We used interrogation windows of size 32×32 pixels or 64×64 pixels with an overlapping of 50%. Their size l_{piv} is about 3 or 6mm. In the vicinity of a bubble, measurements obtained nearer than l_{piv} to the bubble interface have been discarded because of the noise induced by reflexion and bias in PIV estimation due to the presence of a moving object different from the tracers in the interrogation window.

Bubbles evolutions are filmed at 500 frames per second by means of a high-speed camera (Photron APX) with 1280×1024 pixels. The size of the measurement window allows us to observe at least one or two periods of their oscillatory motion. The cell is uniformly illuminated from behind with a stable constant light (Nanolight). The direction of the light is perpendicular to the cell so that the bubble frontier appears clearly as a fine dark line easy to detect (figure 3). A dedicated image analysis algorithm, using a threshold method applied to grey levels, detects the pixels corresponding to the bubble contour projected onto the plane of the cell. From the contour we obtain a description of the in-plane motion and shape and determine the time evolutions of the bubble characteristics (see figure1-b): coordinates $x_b(t)$, $y_b(t)$ and velocities $V_x(t)$, $V_y(t)$ of its centre, projected area S, aspect ratio $\lambda(t) = L/l$ between the major axis L and the minor axis l of the ellipse having the same moments of inertia, angle $\beta_n(t)$ between the minor axis and the x-direction and angle $\beta_v(t)$ between bubble velocity and x-direction. In the following, the bubble is characterized by its averaged equivalent two-dimensional diameter $d = \sqrt{4S/\pi}$. The relative error in the diameter measurement is less than 4%.

For all diameters, the bubble behavior can be described by oscillations of shape and velocity around their mean value (Figure 4) at a single dominant frequency. These oscillations can be reasonably approximated by sine functions, even if secondary harmonics with small amplitudes may appear at largest Ar. The bubble interface evolution is thus described by fitting the following harmonic functions to the measured signals:

$$V_x = V_b + \tilde{V_x} cos(2\omega t + \phi_{vx}), \tag{2.1}$$

$$V_y = \tilde{V_y} cos(\omega t + \phi_{vy}), \tag{2.2}$$

$$\lambda = \lambda_m + \tilde{\lambda} cos(2\omega t + \phi_\lambda), \tag{2.3}$$

$$\beta_n = \tilde{\beta_n} cos(\omega t + \phi_{\beta_n}), \tag{2.4}$$

$$\beta_v = \tilde{\beta_v} cos(\omega t + \phi_{\beta_v}). \tag{2.5}$$

where V_b is the mean rise velocity, λ_m characterizes the mean shape of the bubble around which oscillations may occur, ω is the dominant frequency, and the amplitudes ($\tilde{V_x}$, $\tilde{V_y}$, $\tilde{\lambda}$, $\tilde{\beta_n}$, $\tilde{\beta_v}$) and the phases (ϕ_{vx}, ϕ_{vy}, ϕ_λ, ϕ_{β_n}, ϕ_{β_v}) completely describe the dominant harmonic oscillation.

3. Evolution of mean shape and velocity with Archimedes number

As illustrated in Figure 3 the shape of the bubble evolves markedly when the gas volume is varied. The mean shape aspect ratio λ_m is reported in Figure 5 as a function of Ar. Some instantaneous bubble contours are also reported to illustrate the gradual evolution of the shape. For $Ar \leqslant 600$, λ_m is unity since Bo being smaller than unity (Fig. 2) surface tension is strong enough to keep the shape circular. For larger Ar, λ_m increases as bubbles become elongated and flattened under the action of gravity. Up to $Ar \approx 3.10^3$, λ_m evolves but the mean shape remains an ellipse. Above $Ar \approx 3.10^3$, bubbles adopt more and more complex shapes. The fore-haft symetry is lost for $Ar \geqslant 3 - 4.10^3$ as the rear of the bubble remains concave along an entire oscillation. When $Ar > 7.10^3$, λ_m stops increasing and remains equal to 3. A morphological change has happened, characterized by circular capped bubbles, which have already been observed at high Bo by Collins (1965), Lazarek & Littman (1974) and Bessler & Littman (1987). For any Ar, the aperture angle γ at the rear part of the capped bubbles is nearly equal to $5\pi/8$ in agreement with the estimation of Collins (1965). In the present experimental conditions, we could not generate stable bubbles for equivalent diameters greater than $d \approx 3.5$ cm because such big bubbles broke up.

Varying the Archimedes number allows us to explore a great variety of regimes. The succession of in-plane shapes is similar to that observed for bubbles free to evolve in the three-dimensional unconfined space. It is remarkable that the scaling law giving the velocity of confined bubbles does not depend upon the shape for all the Archimedes numbers that have been explored. As visible in figure 2, the bubble mean velocity for $Ar < 15.10^3$ is well described by the simple law:

$$Re = 0.5Ar. \tag{3.1}$$

This has a major consequence on the role of the liquid films in the bubble dynamics. The average balance of the forces acting on a bubble in the x-direction can be written

$$\rho g \frac{\pi d^2}{4} h = \frac{1}{2}\rho C_D V_b^2 dh + 2\xi \mu V_b / h_f S_f, \tag{3.2}$$

with buoyancy on the $l.h.s$, and on the $r.h.s.$ the drag force exerted by the in-plane motion around the free edge of the bubble plus that exerted by the liquid films. C_D is the drag coefficient, $S_f \approx \pi d^2/4$ the surface of the bubble in contact with a liquid film and h_f the width of the film. On an interface that is free of contaminants, a zero shear-stress boundary condition applies so that the liquid in the films remains almost at rest and does not exert any significant force on the bubble ($\xi \approx 0$). In contrast, contaminated interfaces may be rigidified and a no-slip boundary condition then apply on them. A Couette flow then develops in the films which causes a drag force on the bubble ($\xi = 1$). As we do not use ultra-purified water, partial interface contamination probably exists. This implies that viscous shear stress is non zero in the films ($0 < \xi < 1$). Actually, the force balance reduces to $C_D = 2\pi$ (3.1) which means that the contribution to the drag due to the films is negligible compared to that caused by the flow surrounding the bubble.

We observe a deviation from (3.1) for the smallest bubbles ($Ar < 300$) because their motion is still sensitive to three-dimensional effects. We also note for the largest bubbles ($Ar > 6.10^3$), that a better fit is given by $Re = 0.42Ar$, which corresponds to a systematic relative difference of about 8% with (3.1). Collins (1965) showed that the mean velocity of large two-dimensional bubbles is given by $V_b = 0.5\sqrt{gr_C}$, where r_C is the radius of curvature at the front stagnation point. This scaling is obtained by assuming that the in-plane shape of the bubbles near the stagnation point is well approximated by a circle and

Author	*Ar*	*Bo*	*h/d*	*K*	*k*
Collins (1965)	3900	18	0.55	0.3^{**}	0.545^{*}
Bessler & Littman (1987)	500 to 36.10^3	460 to 520	0.25	0.71^{*}	0.47^{**}
Present work	6.10^3 to 15.10^3	30 to 140	0.06 to 0.03	0.42	$0.43 = 0.42(1.06)^{1/2}$

TABLE 1. Coefficients of the scaling laws for the velocity of 2D semi-circular capped bubbles at high Ar given in the literature. Coefficients are defined by: $K = V_b/\sqrt{gd}$ and $k = V_b/\sqrt{gr_C}$. The values * are directly reported from the measurements, the values ** are obtained assuming that for semi-circular caps d/r_C is related to the measured aperture angles γ by $d/r_C = (4/\pi(\gamma/2 - sin(\gamma)))^{1/2}$

that the flow may be considered potential in this region. For the present largest bubbles, $d/r_C \approx 1.06$, which leads to the theoretical prediction: $Re = 0.485\ Ar$. Therefore, even if the curvature at the stagnation point may explain for a part the decrease of the slope of the curve $Re(Ar)$, it is not sufficient to recover the experimental result. As also mentioned by Collins (1965), a confinement in the y-direction can also reduce the velocity of large two-dimensional bubbles, the dimension of which is not negligible compare to that of the cell. It is however never the case in the present configuration. As shown in Table 1, even at very large Ar for which bubbles are expected to fulfill the assumptions of the theoretical relation derived by Collins (1965), the experimental results published in the literature are scattered and highly sensitive to the Bo and h/d.

To summarize, an important conclusion is obtained about the rise velocity of confined bubbles: for all Reynolds numbers in the range from 150 to 6×10^3, the drag coefficient is constant although bubble size and shape vary significantly. This result contrasts with unconfined bubble for which such a behavior is only observed for spherical capped bubbles at large Bo.

4. Velocity perturbation induced in the liquid

The liquid velocity averaged over the gap $\vec{u}(x, y, t)$ has been explored by PIV for the whole range of Archimedes number. Instantaneous fields of $\vec{u}(x, y, t)$ superimposed to its vorticity Ω_z are plotted in figures 6 to 9 for $200 \leqslant Ar \leqslant 13700$. For all these cases, a strong perturbation develops in the wake of the bubble, the dynamics of which evolves strongly as Ar increases. From $Ar \approx 200$ to 3×10^3, periodic vortex shedding is observed as illustrated in figures 6 and 7. For $200 \leqslant Ar \leqslant 700$, figure 6 shows that the bubbles are not deformed and that, once released, vortices evolve in a vanishing vortex street. As bubbles elongate, the shape of the vortices that are released becomes more and more elongated ellipses, as illustrated by the case $Ar = 1500$ (figure 7). The changes in the vortex shape is related to λ_m by the mechanism responsible for their generation. Vorticity is produced by the fluid rotation around the curved bubble interface and is proportional to both the magnitude of the curvature and the bubble velocity (Batchelor (1990)). The maximum curvature of elongated bubbles is observed near their equator and its magnitude scales as $\lambda_m^{0.5}/d$. The general evolution of the vorticity dynamics when further increasing Ar is revealed by the differences between the instantaneous vorticity fields of cases at $Ar = 1500$ and 2950. At $Ar = 1500$, vortices are released downstream of the bubble, are distant from

each others in the transverse direction and, adopt noticeable inclinations with respect to the x-axis. In contrast, at Ar =2950, they are located close to the bubble, are elongated in the longitudinal direction and, rather close to each others. They are still unsteady, but the trailing vorticity is no longer well organized in detached vortex structures. Except in the region near the bubble, downstream velocities are no longer present in the wake. This leads to a global oscillating wake consisting of two unsteady vortices attached at the equator of the bubble and trailed by a column of ascending fluid entrained by the bubble. This is also observed for cases at Ar =3550 and 4750, which correspond to highly deformable elongated bubbles (figure 8). In this regime, due to the oscillations of the shape and of the inclination of the bubble, a vortex may be generated nearly upstream of the equator as shown for case Ar =3550 (Fig. 8). The magnitude of the non-dimensional vorticity also increases with Ar up to $Ar \approx 3.10^3$, as it can be remarked from the evolution of the scales of Ω_z from figures 6 to 8. For case Ar =4750, a decrease of the non-dimensional vorticity is observed. We shall see later that this is a signature of a change in the oscillating regimes. Then, for the large capped bubbles, the normalized vorticity increases again with Ar (figure 9). The most striking result is that, in between Ar =6950 and 13700, the wake structure changes from non-stationary to stationary. In figure 9 at Ar =6950, a small instantaneous asymmetry of the near wake is observed, which reveals a slight transverse oscillation of the wake. But at Ar =13700, the wake has recovered a stationary state. The instantaneous velocity field is symmetrical, with an attached recirculating wake extending up to $x/d \approx$-1.4 in the longitudinal direction.

Due to confinement, the dynamics of the vorticity produced at the interface presents peculiar features. The vorticity Ω_z can be neither stretched nor tilted, but while it is transported by convection and by diffusion in in-plane directions, it is also attenuated by the shear stresses exerted at walls. The temporal evolution of the vortices has been studied in the range $200 \leqslant Ar \leqslant 2.10^3$ where vortex shedding occurs. We define individual vortices as simply connected regions of vorticity exceeding the ambient noise by a threshold equal to one fourth of the maximum vorticity in this region. Their size d_Ω is defined from their area and their averaged vorticity Ω_m is calculated over the extension of each individual vortex. In figures 10-a and 10-b, these parameters are reported in non-dimensional form: Ω_m is normalized by V_b/d and d_Ω by $d/\lambda_m^{0.5}$ for accounting for the bubble shape. The vorticity vanishes very rapidly behind the bubble passage, in a time independent of Ar related to the diffusive time scale $\tau = h^2/\nu$. This scaling clearly shows that the rapid attenuation of the vorticity is strongly related to the confinement in z-direction. It is not due to an in-plane diffusion of the vorticity as shown by the constant length scale of the vortex achieved during the attenuation process after a short transient (figures 10-b). The experimental law can be approximated by $\Omega_m(t)d/V_b \approx 2exp(-6t\nu/h^2)$. Such an exponential decay confirms that the shear exerted at walls on the liquid flow is the dominant mechanism driving wake attenuation. The evolution of $\Omega_m(t)$ is predicted by the momentum balance averaged over the gap. Assuming that the velocity profile in the z-direction is parabolic and neglecting the in-plane diffusion, the momentum balance writes

$$\rho\frac{\partial\vec{u}}{\partial t} + \frac{6}{5}\rho(\vec{u}.\vec{\nabla})\vec{u} = -\vec{\nabla}P - \frac{12\mu}{h^2}\vec{u}. \tag{4.1}$$

The last term, which is the drag force contribution caused by wall friction, is similar to the term introduced by Gondret & Rabaud (1997). Taking $6/5 \approx 1$, the transport equation of Ω_z is deduced easily,

$$\frac{d\Omega_z}{dt} = -\frac{12\nu}{h^2}\Omega_z, \tag{4.2}$$

the solution of which is $\Omega_z = \Omega_z(0)exp(-12t\nu/h^2)$. The difference between the rates of decay of this solution and that of the experimental law is due to the fact that a parabolic profile has not enough time to develop during the attenuation process. A more rigorous calculation would require to take into account the development of the wall boundary layers during the vortex attenuation. The present analysis is however sufficient to explain the rapid attenuation of the downstream vorticity observed for $200 \leqslant Ar \leqslant 2.10^3$ (figure 10-a).

Figure 11 shows the evolution of the normalized longitudinal liquid velocity $u(x,0)/V_b$ along the symmetry axis of two large bubbles at Ar =6950 and 13700, respectively. (Note that x =0 is the bubble centre). Upstream of the bubble (x >0), the position is normalized by the bubble diameter. Since both Re and $Re(h/d)^2$ are large, the velocity perturbation in front of the bubble is in excellent agreement with the potential flow around a cylinder of radius equal to the bubble radius of curvature at the upstream stagnation point (continuous dark and grey lines). Downstream of the bubble (x <0), the position is normalized by the viscous length, $V_b h^2/\nu$. In the recirculating wake, located approximatively in the region where $\left|x\nu/(V_b h^2)\right| < 0.16$ in both cases, the velocity is greater than V_b. At the rear of the recirculating wake ($-0.4 \leqslant x\nu/(V_b h^2) \leqslant -0.16$), the decay of the velocity perturbation follows an exponential law, $u/V_b = exp(-10x\nu/(V_b h^2))$. The viscous length scale is the one that allows to obtain a decay of u/V_b that is independent of the Archimedes. Farther in the wake, the decrease of the velocity defect turns out to depend again on Ar. The velocity decrease is still exponential, but the slope varies with Ar. This longitudinal evolution is linked to the pressure evolution in the wake. Measurements of the pressure field behind capped bubbles by Bessler & Littman (1987) at high Reynolds numbers (with Re close to 4.10^3 but for larger values of Bo and h/d than in our study) showed the existence of a region of low pressure at the rear of the bubble caused by the the attached vortices. Along the axis of symmetry of the bubble, they found a negligible pressure gradient in the region $-4 \leqslant x/d \leqslant -1$ and a strong positive one in the region $-6 \leqslant x/d \leqslant -4$, which allows to recover the pressure of the unperturbed flow. In our experiment, the location of the slope change ($x\nu/(V_b h^2)$ ≈0.4) corresponds to x/d ≈4 and 3.2 at Ar =6950 and 13700, respectively. We can discuss the decay of the liquid velocity u in a frame moving with the bubble from the x-momentum balance on the axis of symmetry of the wake,

$$\frac{6}{5}\rho V_b \frac{\partial u}{\partial x} = -\frac{\partial P}{\partial x} - \frac{12\mu}{h^2}u, \tag{4.3}$$

In the regions where the longitudinal pressure variation can be neglected, the velocity predicted by Eq. (4.3) is $u/V_b = exp(-10x\nu/(V_b h^2))$. It is in agreement with our experimental observations in the region $-0.4 \leqslant x\nu/(V_b h^2) \leqslant -0.16$ where Bessler & Littman (1987) found a constant pressure.

Farther downstream, the wake is so attenuated that the longitudinal momentum balance on the axis (Eq. 4.3) reduces to an equilibrium between the pressure gradient imposed by the attached vortices and the shear stress at walls. In this region, the pressure coefficient measured by Bessler & Littman (1987) increases so rapidly along the axis that it is possible to fit its evolution by an exponential law, $C_p = (P - P_\infty)/(1/2\rho V_b^2) \approx -1.8 + exp((x - 3\alpha d)/(3.5\alpha d))$, where α is the ratio between the horizontal half-width of the bubble and its diameter. Injecting this pressure gradient into the momentum balance (4.3) and neglecting inertia leads to

$$\frac{u}{V_b} = \frac{V_b h^2}{24\nu}\frac{1}{3.5\alpha d} exp((x - 3\alpha d)/(3.5\alpha d)). \tag{4.4}$$

With such a rapid recovery of the external pressure, an exponential decrease of the velocity is still predicted, but its is lower than in the previous region. This is in remarkable agreement with the behavior observed at Ar =13700 for $x\nu/(V_b h^2) \leqslant$-0.4 (Fig. 11). At Ar=6950, the predicted evolution is less satisfactory, but the simplified balance between a dominant pressure gradient and the shear stress at the walls explains the enhancement of the rate of decrease.

For Ar =6950, figure 12 reports transverse profiles of the liquid velocities u and v normalized by $U_{axis}(x) = u(x, y = 0)$ at several longitudinal locations in the wake ($-3.21 \leqslant x/d \leqslant -1.06$). In the vicinity of the bubble ($x/d \geqslant -2$), the transverse profile of u/U_{axis} does not vary with x in the central region of the wake ($|y/d| \leqslant 0.8$) where the fluid is entrained by the rising bubble. In contrast, in the external region ($|y/d| \geqslant 0.8$), negative values of u are observed. For $x/d \geqslant -2$, the profiles of u/U_{axis} and v/U_{axis} still evolve with the distance x/d, which is the signature of the two attached vortices (fig. 9). Outside the attached wake ($x/d \leqslant -2.4$), both velocity profiles of u/U_{axis} and v/U_{axis} become invariant with x. This invariance is observed beyond the limit of the first region of exponential decrease of U_{axis} ($x/d \geqslant -5.6$). The invariance of the profiles of u/U_{axis} as a function of y/d is a clear indication that momentum diffusion in the plane (x, y) is negligible. Considering the invariant distribution $u/U_{axis}(y/d)$, two transverse regions can be distinguished: (1) a central region ($|y/d| \leqslant 0.65$) where the longitudinal velocity profile is unchanged as compared to that observed for $x/d \geqslant -2$; (2) an external region ($|y/d| \geqslant 0.65$) where it is a linear function of y/d. The longitudinal velocity u vanishes near $|y/d| \approx 1.5$, while the transverse velocity v remains constant and equal to $0.4U_{axis}$ in this external region.

The wakes of confined bubbles are strongly influenced by the shapes of the interface and by the shear stress exerted at the walls. Even if exact transitions were difficult to determine, vortex shedding or unsteady trailing vorticity is observed for $Ar \leqslant 7\times10^3$ -10^4, and stationary wakes for greater Archimedes numbers. In all cases, wakes are attenuated by the confinement and decay very rapidly after bubbles passages. Next section describes the corresponding regimes exhibited by the bubble dynamics.

5. Instability of the bubble motion

The geometrical confinement constrains the path and the deformation of the bubble to in-plane motions. The four degrees of freedom associated to translation, rotation and deformation still permit, however, a great variety of contrasted regimes of bubble dynamics. Figure 13 illustrates these regimes. Successive instantaneous bubble shapes are plotted along their trajectory for different Archimedes numbers in the range from 10^2 to 18×10^3. At Ar =105, the shape of the bubble is circular and the bubble rises at constant velocity on a straight line (fig. 13-a). At Ar = 450 and 1130, ellipsoidal bubbles with negligible shape oscillations show sinusoidal trajectories (fig. 13-b and c). Then, for higher Ar, shape oscillations add themselves to path oscillations (fig. 13-d and e). In this regime, instantaneous shapes are quite elongated. At Ar =2540, the bubble shape oscillates around an ellipse that can be distinguished at specific phases of the oscillation. At Ar =4560, the bubble oscillates with its rear part staying concave all along the oscillation. This loss of fore-haft symmetry is an important feature that happens around $Ar \approx 3 \times 10^3 - 4 \times 10^3$. A region of concave shape curvature is observed at the front part of the bubble when the bubble reaches the extreme transverse positions along its path. The location of this concave curvature moves from the right to the left side in phase with the oscillation of the displacement. Increasing further Ar leads to a regime with strong and complex shape oscillations (fig. 13-f) where two moving regions of concave

shape are always present at the front of the bubble, and where the rear interface remains concave. In this regime the transverse elongation oscillates with a large amplitude. This complex regime is followed by a radical change in the motion. At Ar =9140, the amplitudes of path and shape oscillations are strongly attenuated (fig. 13-g). There still exist two points along the front interface where the curvature changes of sign, but the location of these points is stabilized. At higher Archimedes number, oscillations have completely disappeared (see Ar =18400): the bubble adopts a semi-circular stationary shape and a constant velocity (fig. 13-h). The general features of these successive regimes are in qualitative agreement with the description given by Bush & Eames (1998).

5.1. *Coupled oscillations of path and shape excited by the wake*

For any Archimedes number, the parameters $V_x(t)$, $V_y(t)$, $\beta_v(t)$, $\beta_n(t)$ and $\lambda(t)$ that describe translation, rotation and deformation of the bubble are either steady or periodic with all the same frequency (Fig. 4). The Strouhal number is defined as the non-dimensional frequency of the oscillations, $St = \omega d/V_b$. Its evolution with Ar is plotted in figure 14. It turns out that there is no oscillation below a critical Archimedes number in between 105 and 128, let say $Ar_1 \approx 100$, so that the Strouhal number is equal to zero below this threshold. Above a value denoted Ar_5 that is around 10^4, oscillations also completely vanish because the wakes of the circular capped bubbles are stationary (Fig. 9). Some other values of Ar corresponding to regime transitions are also reported on figure 14. They are not visible on the evolution of the frequency but will appear from those of the amplitudes of the oscillations. In the vicinity of Ar_1, the Bond number is low, the in-plane shape is circular and there is no shape oscillation. The instability of the bubble motion results from that of the wake, which is characterized by regular vortex shedding (Fig. 6 for Ar =200). The transition between steady and oscillatory motions appears in a regime where the confinement ratio h/d is of order unity, which means that the three-dimensional flow induced in the vicinity of the bubbles may still have some influence on the bubble dynamics. The value of Ar_1 is thus expected to depend on Bo and h/d. Kelley & Wu (1997) found that Ar_1 increases from 226 to 332 when h/d decreases from 0.621 to 0.362. The present value of Ar_1 found for $h/d \approx 1$ is therefore consistent with their measurements.

For bubbles of circular or ellipsoidal shape ($Ar \leqslant$1500), the Strouhal number increases up to unity and then reaches a plateau at $Ar \approx$600, indicating that vortex shedding is the cause of bubble path oscillations. The initial increase of St is in agreement with common observations around the onset of the wake instability that develops behind a fixed cylinder as well as behind confined bubbles for various values of h/d (figure 14).

For $Ar \geqslant 1500$, the Strouhal number increases rapidly with Ar to reach approximately 3 at $Ar \approx 10^4$. The increase of St is controlled by the increase of the mean shape ratio λ_m. Two different unsteady regimes are successively observed. For $Ar \leqslant 3 \times 10^3 - 3.5 \times 10^3$, a von Karmán street is present behind the bubbles (Fig. 7). For larger Ar, attached vortices are unsteady but the released vorticity is no longer organized in a von Karmán vortex street (see figure 8). The time-scale of shape oscillations, $\tau_S \approx \sqrt{\rho d^3/\sigma}$, becomes of the same order of magnitude as the period of wake fluctuations. This can promote collaborative action of interface and vorticity dynamics so that vorticity may be enhanced by interface oscillations as observed in figure 8 at Ar =3550.

For all considered Ar, path, wake and shape oscillations are synchronized, a single frequency being observed for all parameters, even for highly deformable bubbles.

5.2. *Overview of the various regimes of oscillations*

Once path instability has appeared ($Ar \geqslant Ar_1$), its development can be discussed by considering the evolutions of the amplitudes and the phase differences of all the parameters which are plotted as a function of Ar in figure 15.

At first, we notice that in the range of Ar where oscillations exist ($Ar_1 \leqslant Ar \leqslant Ar_5$), the amplitudes of the different degrees of freedom do not evolve monotonically. We have defined several values of Archimedes numbers limiting four different regimes of oscillations. The evolution of the amplitudes of the velocity oscillations (figure 15.a) indeed reveals that for $Ar \geqslant Ar_1$ the value of $\tilde{V}_i/V_b$ (i=x or y) increases until $Ar_2 \approx 600$. Then, for $Ar \leqslant Ar_3 \approx 1500$, this amplitude decreases. It is then nearly constant in the range $Ar_3 \leqslant Ar \leqslant Ar_4 \approx 3500$. The last oscillating regime is associated to a final attenuation of the amplitude $\tilde{V}_i/V_b$ when Ar increases until Ar_5. In unconfined situation, the linear growth of the wake instability is generally followed by a non-linear saturation. For confined bubbles, a complex succession of amplifications and attenuations is observed, indicating that both changes in mean shape and confinement have major effects on the dynamics of the instability. The inspection of $\tilde{\lambda}$ and $\tilde{\beta_n}$ show transitions for the same values of Ar as $\tilde{V}_i/V_b$, whereas their evolutions within each regime are different (figures 15.b, 15.c and 15.d). The concordance of the transitions for all the parameters plotted in figure 15 confirms the strong coupling between all the degrees of freedom of the bubble. In the following, the dominant mechanisms for each regime are discussed by considering the effect of confinement and the evolution of the bubble shape.

5.3. *Discussion of the dominant mechanisms*

Regime of initial instability growth: $Ar_1 \leqslant Ar \leqslant Ar_2$.

The mean shape aspect ratio λ_m remains close to unity (Fig. 5) and there is no shape oscillation ($\tilde{\lambda}$ =0, Fig. 15.b) because surface tension is sufficient to keep the in-plane shape nearly-circular ($Bo < 1$). For Ar from 100 to 600, the shape evolves from a circle to an ellipsoid with small eccentricity (Fig. 13). As Ar increases beyond Ar_1, velocity and angular amplitudes $\tilde{V_x}/V_b$, $\tilde{V_y}/V_b$, $\tilde{\beta_v}$ and $\tilde{\beta_n}$ increase suddenly with Ar. Through this first regime of oscillations, the ratio h/d decreases from 1 to 0.3. To discuss the roles of h/d and Ar in the development of the initial instability, it is interesting to compare our results to those of Kelley & Wu (1997) since our confinement ratios are, for$Ar \geqslant$200, similar to theirs. Their experiment suggested that the first path instability corresponds to an Hopf bifurcation when Ar is increased at constant h/d. When h/d is decreased, the critical value Ar_C they found increases, while the growth rate of the amplitude of the y-displacement is given by $\tilde{A}/d \approx C\sqrt{Ar - Ar_C(h/d)}$, with a factor $C \approx 0.0216$ that does not depend significantly on h/d. The evolution of the amplitudes with Ar that we observed is in good agreement with their measurements. This can be seen in figure 15.a where our data closely follow the curve $\tilde{V_y}/V_b \approx C\sqrt{0.5}St\sqrt{Ar - Ar_C}$, which is identical to the above relation for velocity oscillations (represented by the continuous black line for St=1). This confirms the small influence of h/d on the relationship between $\tilde{V_y}/V_b$ and $Ar - Ar_C$. The results are also consistent with the existence of an Hopf bifurcation. Figures 15.c and 15.d reveal that both angular parameters $\beta_v(t)$ and $\beta_n(t)$ oscillate with the same phase and the same amplitude. This means that the bubble keeps a constant orientation relative to the trajectory, both velocity vector and minor axis of the bubble being always aligned.

For these nearly circular confined bubbles, the origin of the path instability is not clear. It is worth recalling that the wake of an unconfined bubble with a clean interface remains stable whatever the value of Re provided the shape is spherical. Following this argument, Kelley & Wu (1997) conjectured that the instability of circular confined bubbles were

caused by interface contamination. It can hardly be the case here since the scaling of the drag force indicates that the interface is not immobilized by contamination. Moreover, the bubbles being circular near the onset of path instability, the vorticity production at interface is not sufficient to generate wake instability. The production and transport of vorticity, which are modified by the confinement, lead to an original mechanism of instability, the exact nature of which still remains an open question.

Regime of attenuation of the first instability: $Ar_2 \leqslant Ar \leqslant Ar_3$.

For $Ar \geqslant Ar_2$, an attenuation of the amplitudes of velocity and angular oscillations is observed. The transition from the previous regime to this one appears progressively, with smooth variations of the amplitudes of all the oscillations with Ar. Whatever the Archimedes number, the bubble shape remains an ellipse of moderate eccentricity ($1 \leqslant \lambda_m \leqslant 1.3$, Fig. 5) and shape oscillations remains small ($\tilde{\lambda} \leqslant$10%, Fig.15.b). There is still no phase difference between $\beta_v(t)$ and $\beta_n(t)$, but their amplitudes differ since $\tilde{\beta_v}$ is lower than $\tilde{\beta_n}$. The attenuation of path oscillations is the striking point of this regime. It is related to the strong vorticity attenuation caused by the wall friction, which happens with a constant time scale $\tau_v \approx h^2/6\nu$ (Fig. 10). The Strouhal number is nearly constant and equal to unity, so that the period of the vortex shedding increases as $\omega^{-1} \approx d^{1/2}$. The life-time τ_v of the vortices thus becomes shorter and shorter compared to the period of vortex detachment, which could explain the decrease of the amplitudes of the oscillations.

Regime of elongated and deformable ellipsoidal bubbles: $Ar_3 \leqslant Ar \leqslant Ar_4$

The transition at Ar_3 occurs when the Bond number is already quite high ($Bo \approx 5$) and is characterized by the sudden appearance of both an important mean deformation and significant shape oscillations (Fig. 5 and 15.b). The discontinuity observed in the evolution of $\tilde{\lambda}(Ar)$ suggests the existence of a bifurcation controlled by the Bond number. The shape oscillations induced by the pressure oscillations in the wake remain for all regimes until Ar_5. For $Ar_3 < Ar < Ar_4$, the mean shape remains an elongated ellipse, with an eccentricity that varies with Ar ($1.5 < \lambda_m < 2.5$, Fig. 5). Considering λ_m as an additional control parameter, it is interesting to examine how the oscillations are influenced by mean bubble deformation. First, from comparison of figures 5 and 14, it is evident that the Strouhal number increases with λ_m. The Strouhal number is approximately given by $0.85\sqrt{\lambda_m}$. It is interesting to notice that this scaling law is similar to that observed for solid axisymmetric bodies with various aspect ratios that are free to move in a liquid at rest (Fernandes *et al.*(2007)). This similarity points out the major role of the aspect ratio in the dynamics of bodies that are free to move. Under data scattering, the non-dimensional amplitudes of the velocity oscillations $\tilde{V_i}/V_b$ are constant for $Ar_3 \leqslant Ar \leqslant Ar_4$. This feature is also related to the increase of λ_m with Ar. An enhancement of the vorticity production is expected as bubble elongation increases. It may however be compensated by the concurrent enhancement of vorticity evacuation by the mean flow and its attenuation by the wall friction.

While $\tilde{\beta_v}$ is nearly constant, it remains lower than the angular amplitude $\tilde{\beta_n}$. The decrease of $\tilde{\beta_n}$ is related to the evolution with λ_m of the added-inertia coefficients in translation and rotation of an ellipse. The flattening of the bubbles increases inertia, which can limit the rotation oscillations as compared to translation ones. Also, an important modification of the phase difference, $\phi_{\beta_v} - \phi_{\beta_n}$, occurs. In agreement with observations for thick disks (Fernandes *et al.*(2005)), the increase of λ_m generates a continuous increase of the phase difference from 0° up to 105°. For the lowest Ar, the inclination of the bubble relative to its path varies but the phase lag being zero, the bubble always approximatetely faces the relative movement. In contrast, the largest bubbles tend to align

their major axes with their trajectories. This modification of the instantaneous inclination of a bubble along its trajectory is known to result from complex modifications of both added-inertia and vortex shedding as the elongation varies (Mougin & Magnaudet (2002), Fernandes *et al.*(2005)).

Shape oscillations appear for ellipsoidal mean shapes before the fore-aft asymmetry is broken. Considering the coupling between unsteady wake and shape oscillations is an important feature of this regime, we can examine the conditions for the matching between the frequency associated to the wake dynamics V_b/d and that of modes $n = 2$ and $n = 3$ of the shape oscillations of a cylindrical bubble of infinite length and circular section. The corresponding periods are given by $\tau_n = 2\pi\sqrt{\rho d^3/(8n(n^2-1)\sigma)}$ (Lamb (1932)). Equating τ_n with d/V_b yields Ar =1450 for n =2, which is in good agreement with Ar_3, the onset of oscillations around a mean ellipsoidal shape. For n =3, this leads to Ar =4090, which is near Ar_4, the Archimedes number corresponding to the disappearance of the bubble fore-aft symmetry.

Regime of complex shapes and intense shape fluctuations: $Ar_4 \leqslant Ar \leqslant Ar_5$

This regime illustrates the two-way coupling between shape/path oscillations and wake instability. The bubbles are very elongated and may adopt complex shapes as illustrated in figures 13.e and 13.f. Shape oscillations are intense as revealed by the large values of $\tilde{\lambda}$ (figure 15.b). Furthermore, the time records $\lambda(t)$ are no longer pure sine functions. The decrease of velocity and angular amplitudes is clear (Fig. 15.a and c). It can be explained by the shape transition and the change in the wake structure that leads to stationary capped bubbles for Ar larger than Ar_5. Shape oscillations provoke the unsteadiness of the wake revealed by velocity measurements (Fig. 8). The trailing vortices remain however attached and are the cause of the permanent concave rear of the bubble. As long as $\tilde{\lambda}$ is large enough path oscillations are observed.

Beyond $Ar_5 \approx 10^4$, all oscillations eventually disappear and stable capped bubbles are observed. The appearance of this asymptotic state where all fluctuations vanish is hard to locate precisely. The biggest isolated bubbles are not easy to produce with our injection system. It is thus difficult to give a precise value for Ar_5 and to analyze if the evolution is a smooth transition or a bifurcation. But the final regime is clearly identified and characterized.

6. Concluding remarks

We have investigated the dynamics of a bubble rising in a Hele-Shaw cell in situations where inertia plays a dominant role. The path and shape dynamics of the bubble in the plane of the cell, as well as the velocity disturbance induced in the liquid phase, have been characterized for $10 \leqslant Ar \leqslant 10^4$. A general description of the various regimes arising from the coupling between wake dynamics and bubble motion has been provided for inertial confined bubbles. When the bubble diameter increases, both the Archimedes number and the Bond number increase, and the evolution of the bubble mean shape is qualitatively similar to the one observed in unconfined geometries. The mean shapes are successively circles, ellipses that are more and more elongated and, finally semi-circular caps. The scaling of the mean velocity indicates, however, that inertia and gravity effects are dominant and stay in a constant ratio over all the range of Archimedes numbers. In contrast, such a behavior is only observed for capped bubbles at very high Archimedes numbers for bubbles free to move in an unbounded domain.

Wake instability is at the origin of path and shape oscillations. The structure and

the dynamics of the wake being strongly dependent on the bubble shape, the coupling between bubble wake and interface oscillations varies as the bubble shape changes. Four different oscillating regimes have been observed in the range $Ar_1 \leqslant Ar \leqslant Ar_5$. Beyond these limits, bubbles have a stationary wake and their motion is stable. They are either small circular bubbles ($Ar \leqslant Ar_1$) or large semi-circular capped bubbles ($Ar_5 \leqslant Ar$) with, in both cases, a straight path. The first regime of instability ($Ar_1 \leqslant Ar \leqslant Ar_2$) appears for bubbles of nearly circular shapes. The observed Hopf bifurcation is not caused by known mechanisms of vorticity production such as critical in-plane curvature or interface immobilization by the presence of contaminants. The instability of the wake results from the particular vorticity dynamics that takes place in a confined geometry. The three-dimensional vorticity distribution in the near vicinity of the bubble interface possibly triggers the instability and the modification of the vorticity balance by the wall friction probably also plays a role. Beyond this initial regime where the instability of the trajectory grows as Ar increases, a second regime appears, where the instability is attenuated. For $Ar_2 \leqslant Ar \leqslant Ar_3$, bubbles are ellipses with moderate eccentricity that experience no shape oscillation and the amplitude of velocity oscillations decreases as Ar increases. This original behavior is explained by the strong attenuation of the trailing vorticity by the wall friction. For $Ar \geqslant Ar_3$, the Bond number becomes rather high so that shape oscillations appear. For $Ar_3 \leqslant Ar \leqslant Ar_4$, bubbles are elongated ellipses exhibiting large shape oscillations. Vortex shedding is still observed and bubble paths oscillate. For $Ar_4 \leqslant Ar \leqslant Ar_5$, bubbles are no longer ellipses since the fore-aft symmetry is broken. They show intense and complex shape fluctuations. Vortex shedding disappears and is replaced by an attached unsteady wake that is dampened when Ar further increases. Path and shape oscillations thus eventually vanish.

By causing a strong attenuation of the wake, limiting motions to the cell plane and imposing strong interface curvature in the transverse direction, the confinement leads to the original regimes revealed by the present investigations. Future works are required to understand the precise physical mechanisms underlying these regimes and to determine the exact nature of the transitions between them. Numerical simulations are probably better suited to achieve this goal.

Acknowledgments. This work was supported by the lab federation FERMaT and by an *ACI Jeunes Chercheurs* of the French Ministry of Research.

REFERENCES

Batchelor, G. K. 1972 Sedimentation in dilute dispersions of spheres. *J. Fluid Mech.* **52**, 245–268.

Batchelor, G. K. 1990 An Introduction to Fluid Dynamics. *Cambridge University Press.*

Bessler W. F., Littman H. 1987 Experimental studies of wakes behind circularly capped bubbles *J. Fluid Mech.* **185**, 137–151.

Bush, J. W. M., Eames, I. 1998 Fluid displacement by high Reynolds number bubble motion in a thin gap. *Int. J. Multiphase Flow* **24, 3**, 411–430.

Clift, R., Grace, J. R., Weber, M. E. 1978 Bubbles, drops and particles. *Academic Press.*

Collins, R. 1965 A simple model of the plane gas bubble in a finite liquid. *J. Fluid Mech.* **22**, 763–771.

Ellingsen K., Risso F. 2001 On the rise of an ellipsoidal bubble in water: oscillatory paths and liquid-induced velocity. *J. Fluid Mech.* **440**, 235–268.

Fernandes P., Risso F., Ern P., Magnaudet J. 2007 Oscillatory motion and wake instability of freely rising axisymmetric bodies *J. Fluid Mech.* **573**, 479–502.

Fernandes P., Ern P., Risso F., Magnaudet J. 2005 On the zigzag dynamics of freely moving axisymmetric bodies *Physics of Fluids* **17**, 098107.

Kelley E., Wu M. 1997 Path instabilities of rising air bubbles in a Hele-Shaw cell *Phys. Rev. Letters* **79, 7**, 1265–1268.

Gondret P., Rabaud M. 1997 Shear instability of two-fluid parallel flow in a Hele-Shaw cell *Physics of Fluids* **9**, 11, 3267–3274.

Lamb H. 1993 Hydrodynamics. (Sixth edition) *Cambridge University Press.*

Lazarek G. M., Littman H. 1974 The pressure field due to large circular capped air bubble rising in water *J. Fluid Mech.* **66**, 673–687.

Lunde K., Perkins R. 1998 Shape oscillations of rising bubbles *Applied Scientific Research* **58**, 387–408.

Magnaudet J., Eames I. 2000 The Motion of High-Reynolds-Number Bubbles in Inhomogeneous Flows *Ann. Rev. Fluid Mech.* **32**, 659–708.

Maruvada S. R. K., Park C. W. 1996 Retarded motion of bubbles in HeleShaw cells *Physics of Fluids* **8**, 12, 3229–3233.

Maxworthy T., Gnann C., Krten M. and Durst F. 1996 Experiments on the rise of air bubbles in clean viscous liquids *J. Fluid Mech.* **321**, 421–441.

Mougin G., Magnaudet J. 2002 Path instability of a rising bubble *Phys. Rev. Letters* **88, 1**, DOI: 10.1103/PhysRevLett.88.014502.

Mougin G., Magnaudet J. 2006 Wake induced forces and torques on a zigzagging/ spiralling bubble *J. Fluid Mech.* **567**, 185–194.

Roudet M., Billet A. M., Risso F., Roig V. 2011 PIV with volume lighting in a narrow cell: An efficient method to measure large velocity fields of rapidly varying flows *Experimental Thermal and Fluid Science* **vol. 35, issue 6**, 1030–1037.

Segré G. and Silberberg A. 1962 Behaviour of macroscopic rigid spheres in Poiseuille flow Part 2. Experimental results and interpretation *Physical Review Letters* **14**, 136–157.

Shew, L., Poncet, S., Pinton, JF. 2006 Force measurements on rising bubbles. *J. Fluid Mech.* **569**, 51–60.

Taylor G. I., Saffman P. G. 1959 A note on the motion of bubbles in a HeleShaw cell and porous medium *Q. J. Mech. Appl. Math.* **12**, 265–279.

Williamson C. H. K. 1988 Defining an universal and continuous Strouhal-Reynolds number relationship for the laminar vortex shedding of a circular cylinder *Physics of Fluids* **31**, 10, 2742–2744.

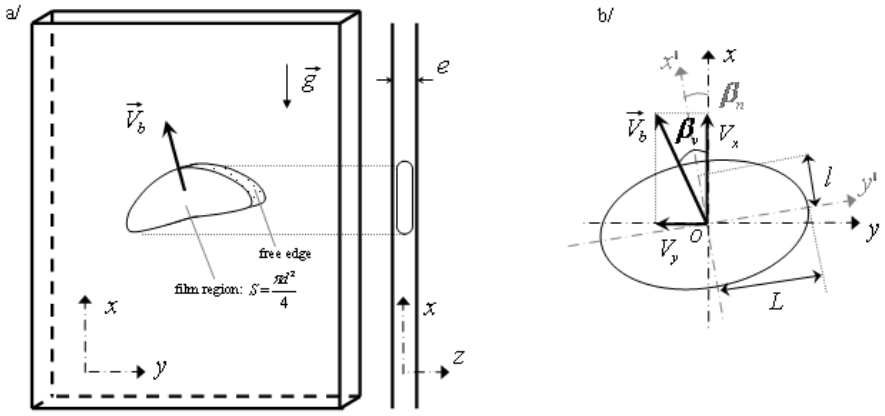

FIGURE 1. Parameters used to describe bubble trajectory and shape

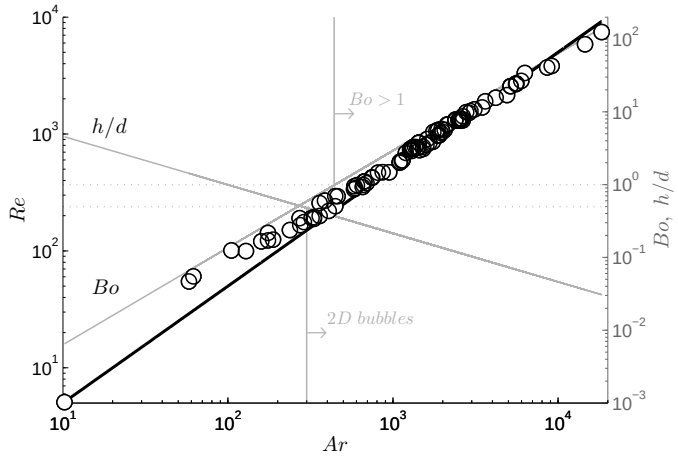

FIGURE 2. Evolutions of Reynolds number, Bond number and confinement ratio h/d with Archimedes number

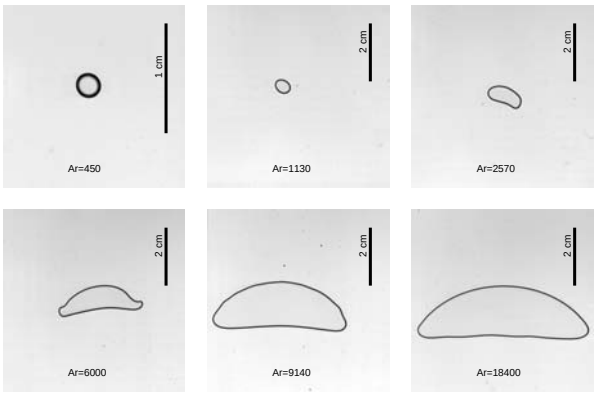

FIGURE 3. Snapshots of bubbles when Ar is varied.

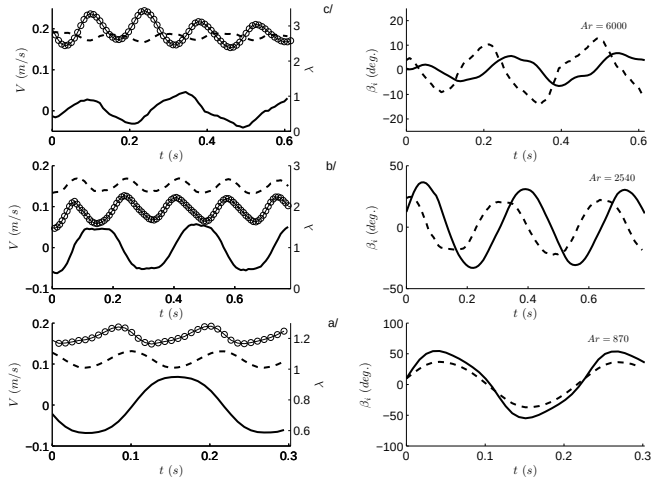

FIGURE 4. On the left side: Time variations of bubble velocity components (V_x, V_y) and deformation (λ) (dotted line V_x, continuous line V_y, continuous line with open circles λ). On the right side: Time variations of the characteristic angles (β_v, β_n) (dotted line : β_v, continuous line : β_n). Three different cases are plotted with the Archimedes numbers: Ar=870 (a), 2540 (b) and 6.10^3 (c).

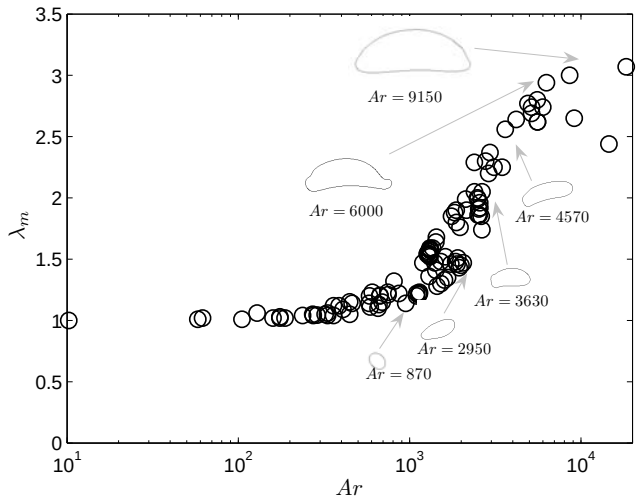

FIGURE 5. Evolution of the mean aspect ratio with the Archimedes number

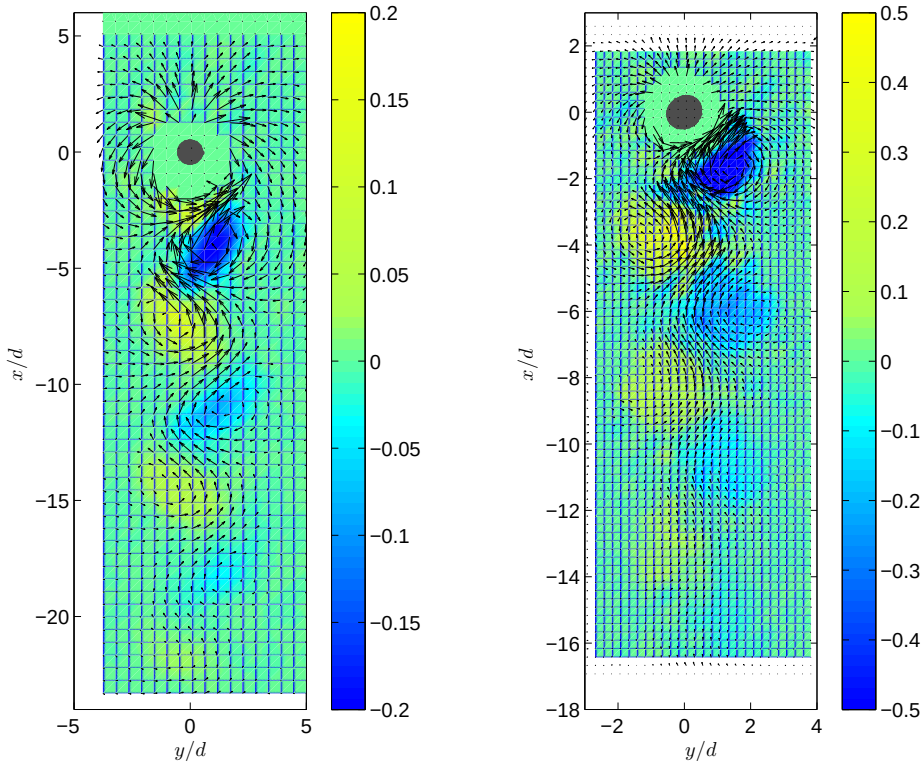

FIGURE 6. Velocity and vorticity around bubbles at Ar =200 (left) and 700 (right). (Vorticity is normalized by V_b/d. Measurements near the interface have been discarded.)

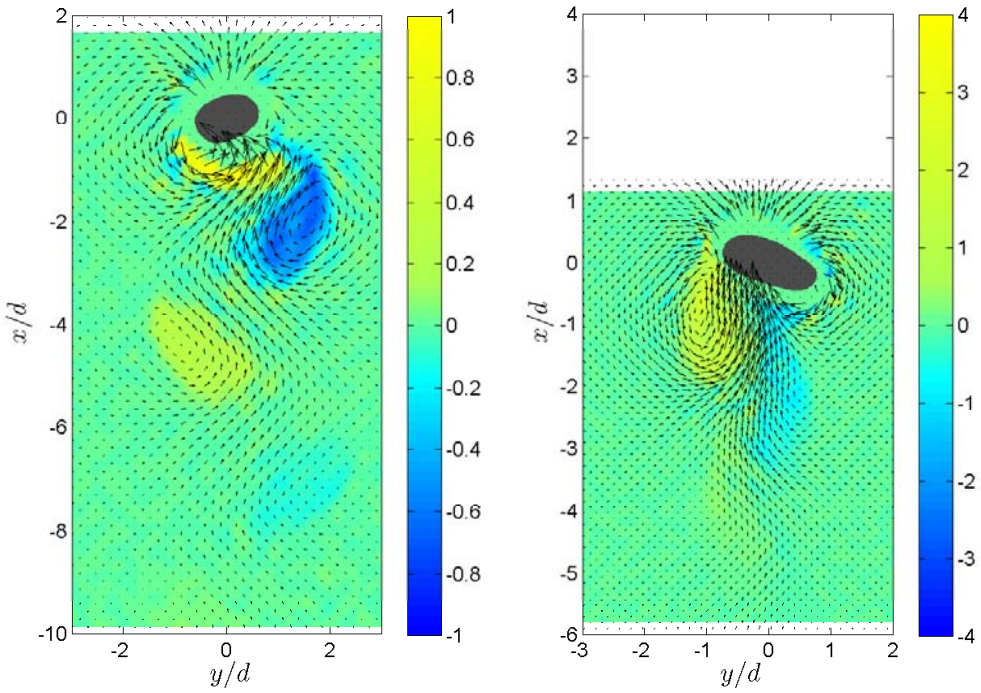

FIGURE 7. Velocity and vorticity around bubbles at Ar =1500 (left) and 2950 (right). (Vorticity is normalized by V_b/d. Measurements near the interface have been discarded.)

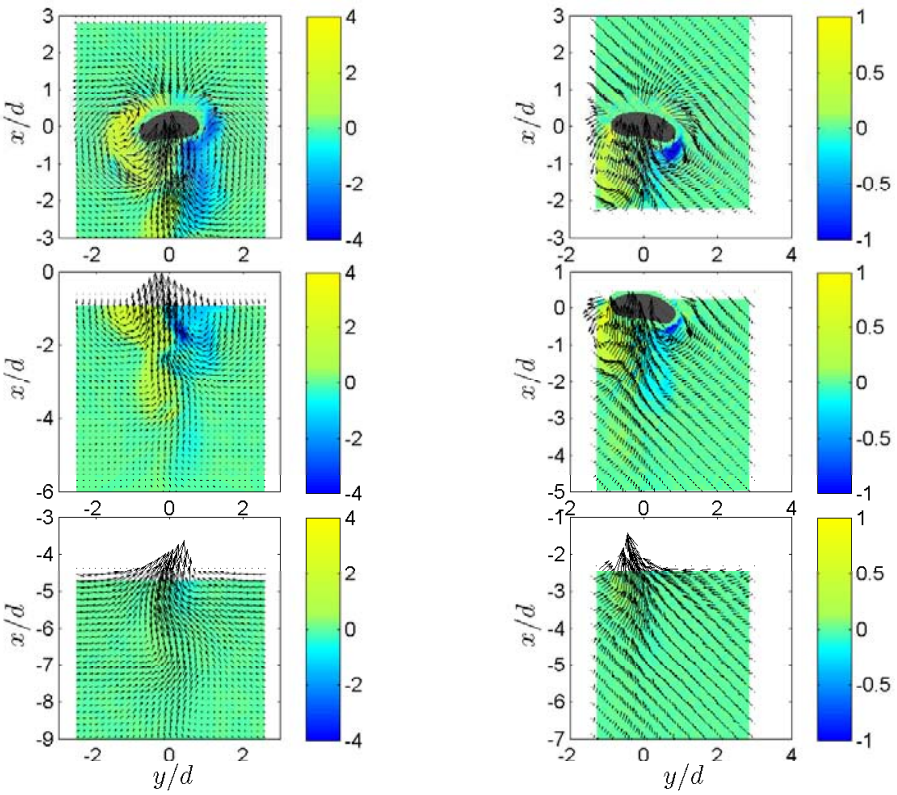

FIGURE 8. Velocity and vorticity around bubbles at Ar =3550 (left) and 4750 (right). (Vorticity is normalized by V_b/d. Measurements near the interface have been discarded.) (For each bubble we have reported three successive velocity fields during or after the bubble passage. The x-coordinate has been translated assuming the bubble is rising at constant velocity.)

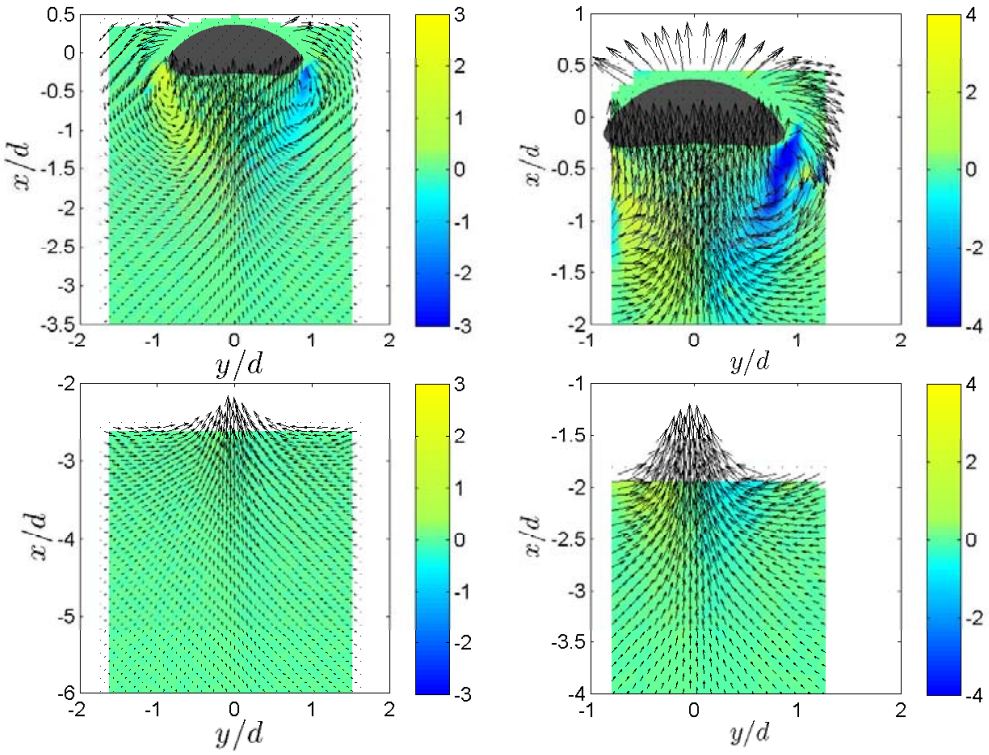

FIGURE 9. Velocity and vorticity around bubbles at Ar =6950 (left) and 13700 (right). (Vorticity is normalized by V_b/d. Measurements near the interface have been discarded.)(For each bubble we have reported two successive velocity fields at a fixed measuring window. The x-coordinate has been translated assuming the bubble is rising at constant velocity.)

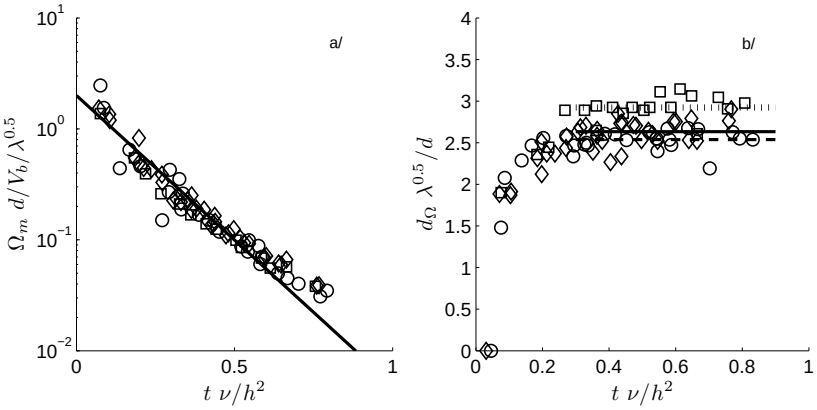

FIGURE 10. a/ Decay of released vorticity with time for various Archimedes numbers. (dark line is $\Omega_m d/(V_b\lambda^{0.5}) = 2exp(-6t\nu/h^2)$). b/ Temporal evolution of the size of the released vortices for various Archimedes numbers. (Ar =700 (□ and bold dotted line), 1250 (⋄ and continuous line), 1950 (○ and dotted line)).

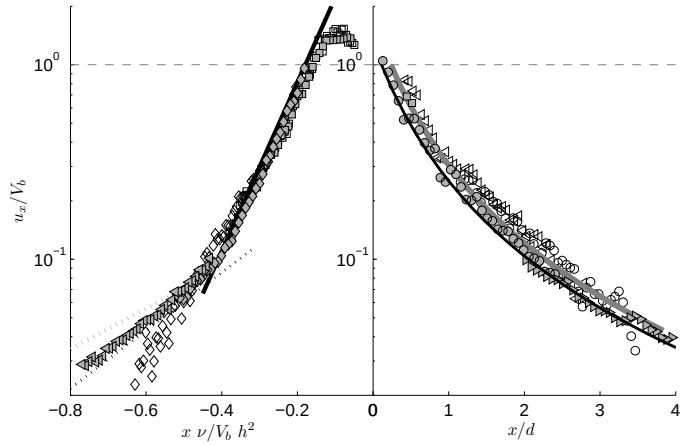

FIGURE 11. Evolution of the longitudinal velocity along the axis of a bubble at Ar =6950 (open symbols) and 13700 (grey symbols). (Distances are normalized by $V_b\ h^2/\nu$ on the left in the wake and by d on the right in front of the bubble). At the front of the bubble we have reported the potential solution for the flow around a cylinder with a radius equal to the radius of curvature at the stagnation point r_C. As the ratio between r_C and d is not perfectly constant between both experimental cases, there is a small difference between both potential solutions. The law of exponential decay $\approx exp(-10t\nu/h^2)$ is plotted in dark in the region of the wake. In dashed lines the law $\frac{u}{V_b} = \frac{V_b h^2}{24\nu}\frac{1}{3.5a}exp((x-3\alpha d)/(3.5\alpha d))$ where the ratio between the half horizontal width of the bubble and its diameter has been measured in figure 9: $\alpha = 0.8$ for Ar =6950 (in black) and $\alpha = 0.9$ for Ar =13700 (in grey).

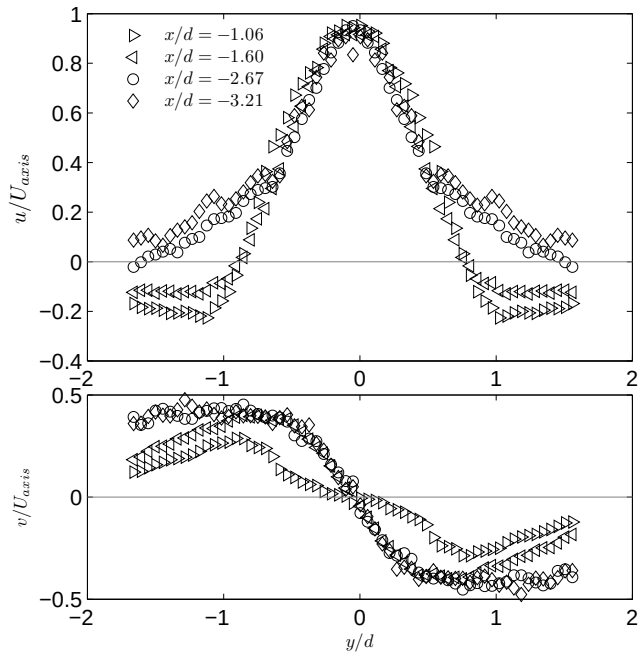

FIGURE 12. Transverses profiles of the velocity in the liquid around a bubble at Ar =6950. x/d = -1.06 (▷), -1.60 (◁), -2.67 (○), -3.21 (◇).

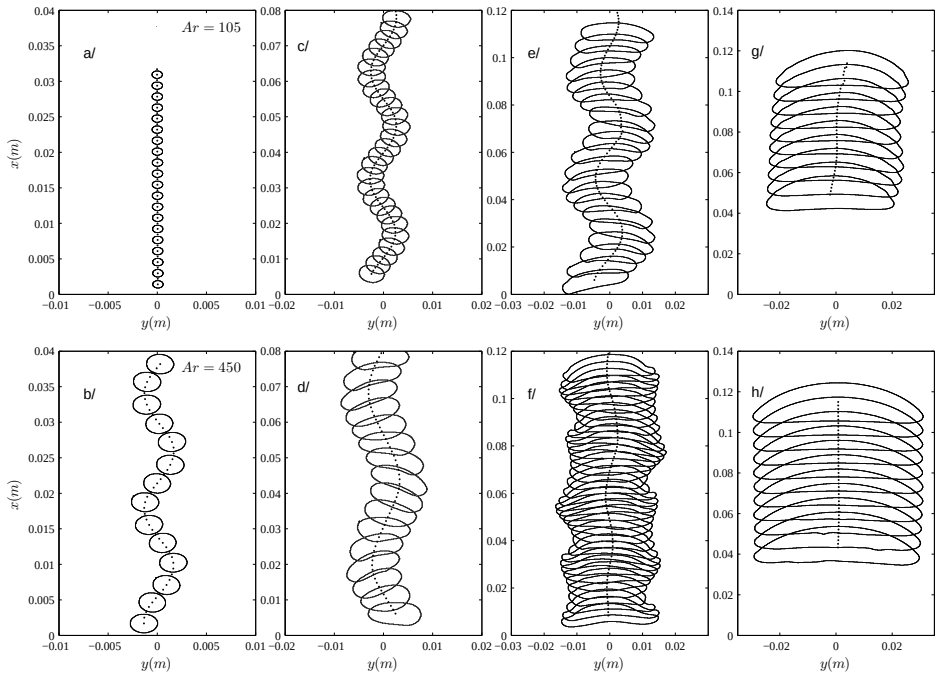

FIGURE 13. Various regimes of shape and path oscillations. The contours are plotted with an time interval δt. a/ Ar =105 δt=16ms, b/ Ar=450 δt=32ms, c/ Ar=1130 δt=24ms, d/ Ar=2540 δt=32ms, e/ Ar=4560 δt=32ms, f/ Ar=6.10^3 δt=16ms, g/ Ar=9140 δt=32ms, h/ Ar=18400 δt=32ms

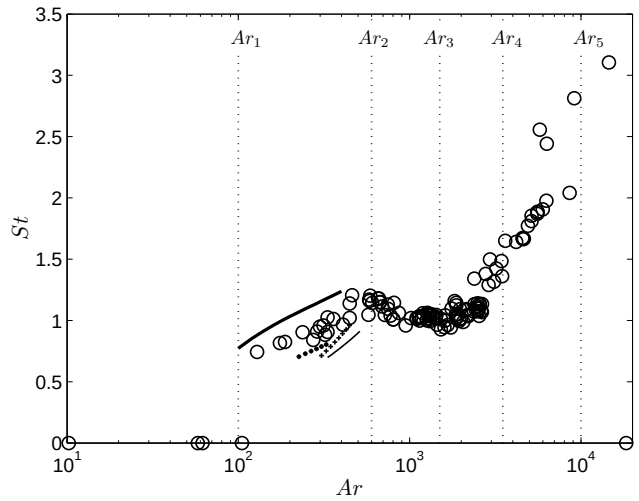

FIGURE 14. Strouhal as function of Ar. (Present experiments: ∘, results of Williamson (1988) for a fixed cylinder: black line in bold, results of Kelley & Wu (1997) at 3 fixed values of h/d: 0.621 (•), 0.448 (+) and 0.362 (black line))

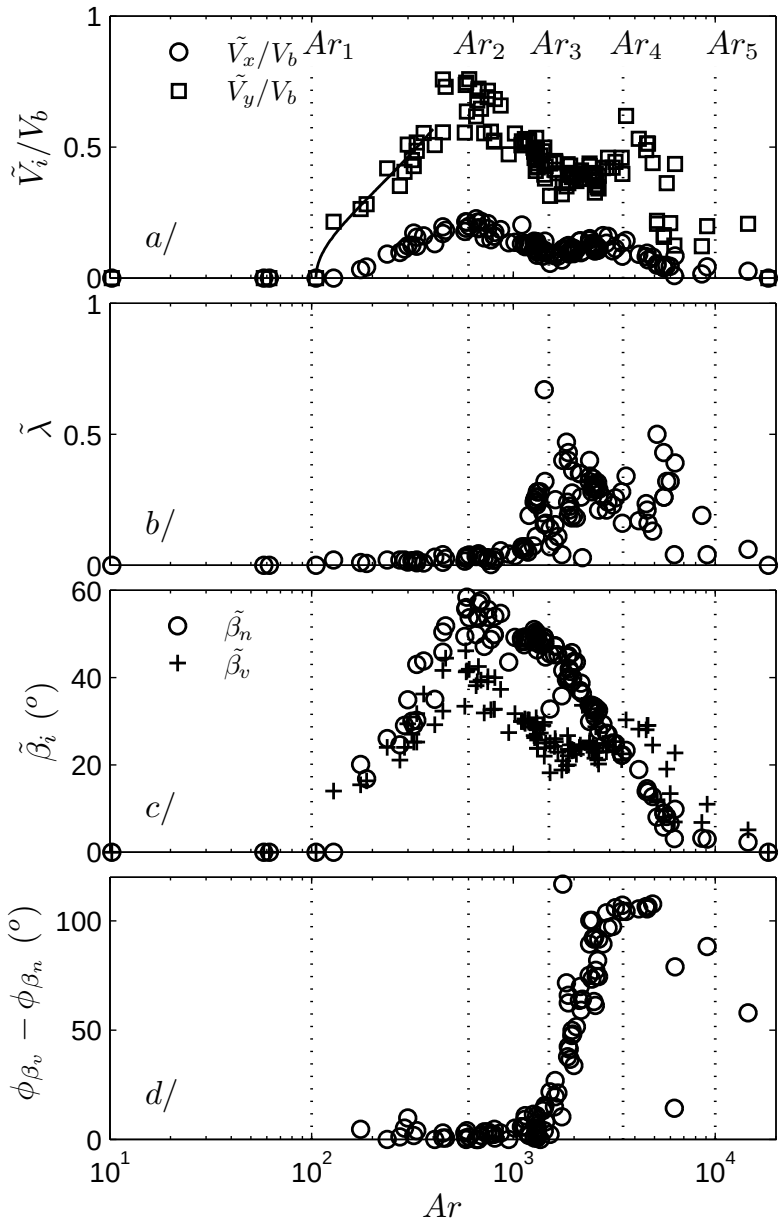

FIGURE 15. Amplitudes and phases of the oscillations as function of Ar. a/ Velocity fluctuations normalized by the mean velocity V_b (in continuous line the evolution observed by Kelley & Wu (1997)); b/ Oscillations of shape; c/Amplitudes of angles; d/ Phase difference